MuPET : Multiphysics and Noise Modelling Approach for Synthetic PET Data Generation – A Methodological Evaluation for 3D Printed Phantom Design

Sai Kiran Kumar Nalla[1, *], Quentin Maronnier[2], John A. Kennedy[3,4], Sebastian Uppapalli[5], Olivier Caselles[2,6]

1. IUTC - Institut universitaire du cancer de Toulouse, Universite de Toulouse, Toulouse, France
2. Department of Medical Physics, Oncopole Claudius Regaud, IUTC Oncopole, Toulouse, France
3. Department of Nuclear Medicine, Rambam Health Care Campus, P.O.B. 9602, 3109601 Haifa, Israel
4. Ruth and Bruce Rappaport Faculty of Medicine, Technion Israel Institute of Technology, Haifa, Israel
5. Department of Aerospace and Mechanical Engineering, École Centrale School of Engineering, Mahindra University, Hyderabad, India – 500043
6. Tachyons SAS, Toulouse, France

***Correspondance : sai-kiran-kumar.nalla@univ-tlse3.fr**

ORCID IDS :

Sai Kiran Kumar Nalla : 0000-0002-8044-6330

Quentin Maronnier : 0000-0002-2266-9122

John A Kennedy: 0000-0002-2043-4397

Sebastian Uppapalli: 0000-0003-0805-7290

Olivier Caselles: 0000-0002-5404-5066

Abstract:

3D-printed phantoms offer customizability and cost-effective surrogates for research in medical imaging but their iterative design and testing often requires demand significant time and resources. In the context of positron emission tomography imaging, the design restrictions are furthermore due to use of radioactive tracers. Although simulations can be helpful in this optimizing the designs in early phases, most commonly used toolboxes are either computationally intensive or retrospective, capable of being performed only after initial prototyping. In this study we aim to introduce MuPET (Multiphysics PET), a computationally efficient framework to generate realistic synthetic PET data to accelerate the design, optimization, and evaluation of novel 3D-printed phantoms. The framework combines multiphysics based diffusion-reaction modelling to generate simulated activity maps followed by the integration of a scanner-specific pseudo-Poisson noise model and spatially variant Gaussian blurring to emulate noise characteristics. As a proof-of-concept, MuPET was validated against acquisition PET data acquired from a custom 3D-printed phantom and conventional synthetic lesion insertion method. The custom phantom consisted of 6 spherical targets (2 diameters – 15mm, 20mm x 3 target to background ratios – 2:1, 2.5:1, 3.33:1) and 3 non target 3D printed inserts. All the acquisitions were performed based on standard imaging guidelines. For the evaluation - volume averaged activity (in MBq), recovery coefficient (RC) and target contrast ratio (TCR), coefficient of variability (CoV) are utilized as metrics. Additionally, extracted activity profiles and ROI based histograms were compared for overlap. Wilcoxon rank sum test was utilized for statistical comparison of activity profiles with significance of $p \sim 0.05$. Variability between volume averaged activity for computational geometry and physical phantom was less than 1.5%. RC_{mean}, TCR_{max} showed strong agreement with both acquisition and conventional simulation values falling within 10% bounds while RC_{max} showed slight underestimation. CoV values for MuPET (3.9-4.04%) closely matched acquired PET (3.75-3.91%). Activity profiles effectively captured the transition across various regions of the phantoms and the histogram jaccard overlap for targets was found to be 80% for 20mm and 60% for 15mm. No statistically significant differences were observed for the target activity profiles with p-values of ≥ 0.54 (vs acquisition) and ≥ 0.19 (vs conventional simulation). A notable achievement is MuPET's computational efficiency, requiring approximately 10-15 minutes for a 35-minute simulation, alongside its flexibility in handling custom phantom designs. This faster, more adaptable pipeline aids in the design, optimization, and evaluation of novel 3D-printed phantoms.

Abbreviations used in the article:

AAPM	American Association of Physicists in Medicine
ABS	Acrylonitrile Butadiene Styrene
AC	Activity Concentration in kBq/ml
Acq	Acquisition
ANOVA	Analysis of Variance
BPL	Bayesian penalized-likelihood reconstruction
$\mathbf{C_i}$	Concentration along direction i in mol/m^3
COV	Coefficient of Variability
CTAC	Computed Tomography Attenuation Correction
CTS	Counts
D	Diffusion Coefficient
DICOM	Digital Imaging and Communications in Medicine
DMI	Discovery MI
EM	Expectation-maximization
FAST PET	Fast analytical simulator of tracer PET
FDM	Fused Deposition Modelling
FDG	Fluorodeoxyglucose
FOV	Field of View
FWHM	Full Width at Half Maximum
HU	Hounsfield Units
ISL	Inserted Synthetic Lesion
KDE	Kernel Density Estimation
$\mathbf{K_{scale}}$	Noise Scale Parameter
MuPET	Multiphysics PET
MVR	Mean to Variance Ratio
n	Normal Vector
$\mathbf{N_A}$	Avogadro Number
NEMA	National Electrical Manufacturing Association
PET / CT	Positron Emission Tomography / Computed Tomography

PETSTEP	PET Simulator of Tracers via Emission Projection
PSF	Point spread function
PVE	Partial volume effects
QC	Quality Control
RC	Recovery Coefficient
ROI	Region of Interest
SMART PET	SiMulAtion and ReconsTruction PET
$\mathbf{S_{scanner}}$	Scanner sensitivity in cps/kBq
$\mathbf{T_{1/2}}$	Half Life of Radiotracer in min
TBR	Target to Background Ratio
TG 126	Task Group 126 Report
TOF	Time of Flight
$\mathbf{T_{scan}}$	Scan Duration
VOI	Volume of Interest
$\mathbf{V_{voxel}}$	Voxel Volume in mL
λ	Decay factor in s^{-1}
μ	Mean
σ	Standard Deviation
ρ	Density of radiotracer in g/mL
ϕ	Diameter

Introduction:

Positron emission tomography (PET) in combination with computed tomography (CT) imaging offers unique insights in early diagnosis of cancer by combining functional (metabolic) and structural (anatomical) information [1–3]. Traditionally, simpler systems such as phantoms are designed for benchmarking of quantitation and image quality tests across generations of scanners [4–6]. Additionally, they are also majorly used for scanner calibration and testing of new algorithms. However, current phantoms fall short in customizability necessary to mimic anatomically realistic conditions accurately [7–9]. Three dimensional (3D) printing has emerged as a key tool in this regard to create more realistic phantoms at a lower cost [8–12]. This facilitates rapid prototyping of complex models, allowing for the inclusion of tissue heterogeneity and detailed lesion morphologies [13–15]. Adaptability of 3D printed phantoms across facilities for standardization and harmonization studies is also established [16–18].

Parallelly, PET simulations are powerful tools utilized for generating synthetic data under a controlled environment. These simulations can broadly range from simplified analytical models, which offer computational speed, to highly detailed Monte Carlo simulations, which meticulously track individual particles through complex geometries, albeit at significant computational cost [19–24]. The compatibility of customized 3D printed phantoms with existing simulation methods is proven [9]. Integrating simulations directly within 3D design workflow allows for optimization and testing of various configurations and features virtually before engaging in physical fabrication. But a significant limitation currently concerns their retrospective nature i.e. the application of such simulations is only possible after the physical model has been developed. Current techniques for introducing synthetic lesions necessitate an initial baseline PET scan [23,24]. Further, the complexity associated with the design and material properties of 3D-printed components adds to the computational expense to simulations, especially when using particle tracking or monte carlo techniques [19]. Additionally, the variation of CT attenuation properties with aging of the print requires continuous empirical data to ensure accurate representations [8]. Although simulated noise free activity distributions can be created and transformed into PET images [20–22], most current frameworks are not flexible enough for custom designs which do not have the appropriate digital models available. This necessitates an alternative simulation approach that can be used within 3D modelling framework. Multiphysics modelling coupled with compartmental modelling particularly those employing tracer kinetics or reaction-diffusion models, can help in developing time activity curves and activity distribution maps [25–29]. Mass transport models are being widely applied in many fields, including drug delivery, medical device testing and also PET/CT applications [26,30–32]. Given the mechanical nature of phantoms, this approach can be readily integrated into the 3D design framework as the parameters can directly correlate with the modelling conditions used in these simulations. Additionally, these models can be easily coupled with fluid flow modelling thus enabling simulation frameworks for

dynamic imaging. The use of such models for PET imaging is not yet widely explored because the activity distributions generated by multiphysics simulations are inherently noise-free approximation, as they are uninfluenced by scanner characteristics, reconstruction algorithms, or positron physics. To derive quantitative data that more closely resembles real-world scans, synthetic noise or a simplified PET scan reconstruction must be introduced to these simulated maps [33,34]. Faster PET reconstruction based simulations such as PETSTEP (PET Simulator of Tracers via Emission Projection) [22] or SMART PET (SiMulAtion and ReconsTruction) [20] and FAST PET (fast analytical simulator of tracer) [21] use sinogram based methods with CT based attenuation correction. In such methods, the activity map is forward projected using a Radon transform and all steps are performed in the projected domain. An alternative method is, synthetic noise modelling [33,35] built empirically based on uniform phantom scans specific to a scanner and reconstruction settings. This method can be carried out in both image and projected domains. While PET noise is predominantly modelled as Poisson due to the underlying physics [34], actual PET scans often deviate from this assumption [36], typically exhibiting a variance higher than their mean (when measured in Bq) [33,34,37]. To address this limitation, multiple approaches have been proposed to include a pseudo-poisson noise model with a count scaling parameter [35], a negative binomial model [34,35], a Poisson regression model [37], a gamma distribution model [38], and a noise power spectrum model [33]. Commonly, all these approaches scale the mean to variance ratio (MVR) in their own way, with some being less reliant on empirical data than others. It's also been reported that noise in clinical images is a combination of Poisson and Gaussian components and expectation-maximization (EM) reconstruction algorithms are often better represented by a gamma distribution [38].

In this work, we introduce MuPET (Multiphysics PET), a new framework that employs diffusion-reaction modelling of tracer concentrations with scale factor based pseudo poisson noise model deployed in image domain. The framework was carried out and validated for a custom 3D printed phantom design adapted from [8,17]. A spatially variant gaussian model to represent the scanner's point spread function (PSF) for resolution modelling was used in noise modelling. Additionally, a conventional synthetic lesion insertion method [24] was also used for benchmarking. We present a simplified and fast approach that can significantly aid in the design of novel phantom features.

2. Methods:

2.1 Phantom Acquisitions and Synthetic Lesion Insertion:

A custom-designed phantom (**Fig. 1**.**a**), adapted from [8], was utilized for this study. It consists of a Jaszczak cylinder phantom with nine 3D printed permeable cubes (40 mm) of acrylonitrile butadiene styrene (ABS) with varying dilutions (50%, 60%, and 70%). Six of these cubes incorporated spherical targets (20 mm and 15 mm in diameter), while the remaining served as homogenous cubes with no targets (**Fig. 1**.**b**). The phantom was pre-filled with a water/soap solution 4-5 hours prior to image acquisition. Fifteen minutes before scan, 56.7 MBq of ^{18}F-FDG

radiotracer was injected into estimated 6.2 L volume. All scans (**Fig. 1.c**) were performed using single bed position on a Discovery MI PET/CT platform (*GE Healthcare, Chicago, IL, USA*) across three consecutive frames 300 seconds each with a single CTAC (CT Attenuation correction). The activity at the time of scan was decay-corrected relative to the injected activity and residual in syringe. PET data were reconstructed into a 384 x 384 x 89 volume with voxel spacing of [1.042, 1.042, 2.8 mm] using Q.Clear FX BPL (*Bayesian penalized-likelihood reconstruction with regularization parameter, TOF* , β: 550). Detailed phantom preparation protocol and acquisition parameters can be found in [17].

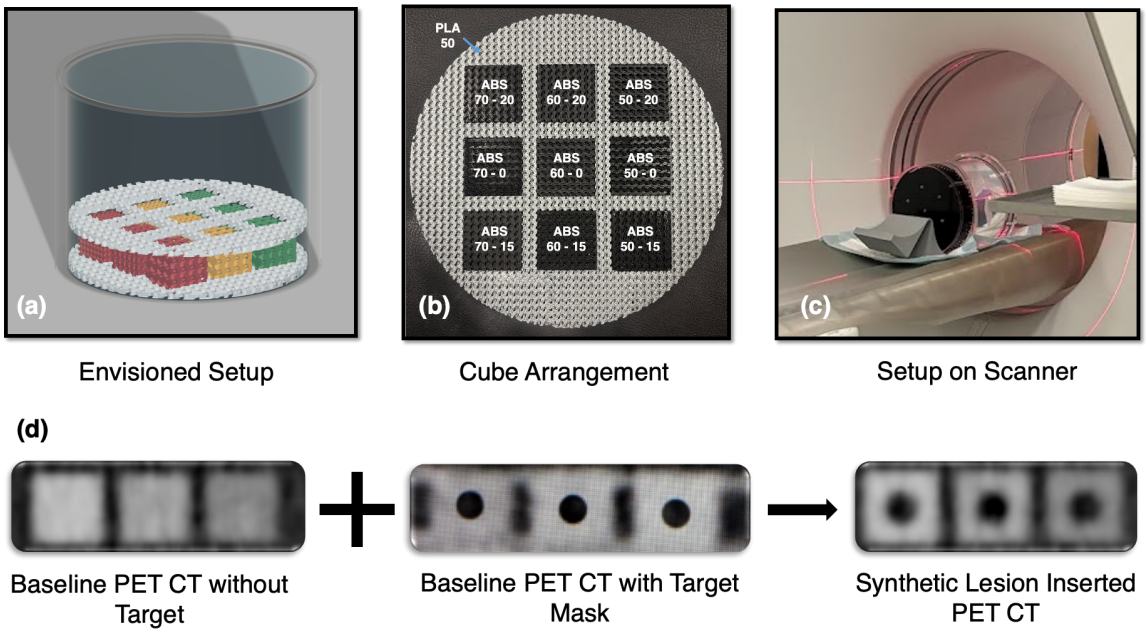

Fig.1 (a) 3D rendering of the adapted phantom design; (b) Arrangement of cubes – (Notation: Percentage of ABS – Target size); (c) Bed leveling on PET/CT scanner; (d) Summarized workflow of synthetic lesion insertion

Subsequently, synthetic lesion insertion was performed based on a previous workflow [24] using Duetto (*GE Healthcare, Chicago, IL, USA*) [23,39]. Spherical binary masks of 15 and 20mm were created and positioned on the homogeneous cubes (No target) in the acquired PET images (**Fig. 1.d**). Inserted synthetic lesions (ISL) were created by specifying the target to background activity ratio (TBR) with respect to the homogeneous cube measurements to the generated masks which were converted into simulated sinogram. This was added to the experimental sinogram and a final lesion inserted images are generated through reconstruction process and parameters matching the acquisitions.

2.3 MuPET Framework:

The MuPET (Multiphysics PET) framework introduced here presents a computationally efficient pipeline for simulating PET image data. This approach combines COMSOL Multiphysics® (*COMSOL Inc, Stockholm*) based tracer distribution modelling with a synthetic noise modelling post-processing workflow.

2.3.1 Numerical Modeling:

Conservative mass transport within the phantom was modelled using a simplified diffusion-reaction equation (Eq. 1). This assumes passive movement of the radiotracer driven by concentration gradients, coupled with a first-order radioactive decay process. The phantom geometry for the numerical simulation was constructed based on manufacturer dimensions adjusted to measured fillable volume as represented in **Fig.2.a**. The overall phantom volume was faithfully replicated based on weight to volume conversion, while the precise dimensions of the cubes and spherical targets were extracted directly from the design files used for 3D printing.

$$\frac{\partial C_i}{\partial t} = \nabla.(D.\nabla C_i) - (\lambda * C_i)\ ;\ \lambda = \frac{\log 2}{T_{1/2}} \qquad (1)$$

Where C_i is concentration in mol/m^3, D is Diffusion Coefficient (m^2/s), λ is decay factor (1/s), $T_{1/2}$ is the half-life (s)

Initial activity concentration in background (AC_{in}) for the simulation were derived from injected activity divided by the volume. These initial concentrations were further modulated to represent distinct contrast levels within the cubes for dilutions corresponding to 50%, 40%, or 30% of the reference activity concentration (i.e., 0.5 × AC_{in}, 0.4 × AC_{in}, or 0.3 × AC_{in}, respectively). Activity concentration in kBq/mL were converted to mol/m^3 based on (Eq. 2). A no-flux boundary condition was used as an approximation on the outer walls of the cylinder using (Eq. 3), leading to all activity conservation within the domain. Notably, injection and initial tracer uptake were not considered in this framework.

$$C_i = \frac{AC_i}{(\lambda * N_A)}\ ;\ N_A = 6.02 \text{ x } 10^{23} \qquad (2)$$

Where N_A is Avogadro's Number in mol^{-1} and AC is Activity Concentration in kBq/mL

$$-n\,.(D.\ \nabla C_i) = 0 \qquad (3)$$

All material properties within the numerical model were assumed to be analogous to those of ^{18}F-FDG and water and in instances where specific properties were not readily available corresponding values for glucose were adopted as a reasonable approximation. The properties used are as follows, Density of the fluid (ρ) : 1.00 g/mL, Diffusion Coefficient of FDG in water (D) : 6 x 10^{-10} m^2/s is adapted from value of glucose **[40]**, Half-Life of tracer ($T_{1/2}$) : 110 minutes **[41]**. To validate the modelled geometry, volume averaged activity (MBq) in the domains was compared with decay corrected values from DICOM metadata. The computational domains were discretized based on grid independency performed on average of concertation's sampled at 726 (11 x 11 x 6) different locations with an acceptable threshold of 5% across 3 grid

sizes for numerical stability. The simulations were computed for 35 minutes with a step size of 1 min using an iterative solver.

2.3.2 Synthetic Noise Modeling:

A simplified noise modelling approach was considered which accounts in PET physics noise and some scanner resolution effects, with reconstruction induced effects out of current framework. All the noise modelling was performed in the image domain in contrast to projected (sinogram) domain conventionally used.

(a) The simulated activity maps $AC_{Simulated}(x,y,z,t)$ in kBq/mL, were exported as a 4D volume with spatial dimensions of matching the experimental scan volumes 383 x 383 x 89 (1.042 x 1.042 x 2.8 mm^3). Additionally the maximum and minimum values of activity concentration within computational domain are exported as function of time $AC_{Max}(t)$ and $AC_{Min}(t)$.

(b) Upon import into MATLAB (*MathWorks INC, MA, USA*), an initial data cleaning process was performed to address any corrupted values by replacing them through interpolation or clipping based on minimum and maximum values from ideal map. The volumes are reoriented if necessary to the Field of View (FOV) of actual scan and separated into individual 3D volumed.

(c) To introduce some scanner effects, the activity maps were first converted into expected counts CTS (x,y,z). This conversion utilized the T_{scan}: scan duration (in seconds), $S_{scanner}$: scanner's sensitivity (in counts per second per kilobecquerel, cps/kBq) adapted from NEMA (National Electrical Manufacturers Association) [42] and V_{voxel}: voxel volume in mL

$$CTS(x,y,z) = AC_{simulated}(x,y,z) * S_{scanner} * T_{scan} * V_{voxel} \qquad (4)$$

(d) The resulting count volume $CTS(x,y,z)$ was then subjected to a pseudo poisson approach: the counts were multiplied by an adjustable scale factor to generate $CTS_{scale}(x,y,z)$, after which Poisson noise was generated to introduce PET physics based noise $CTS_N(x,y,z)$, then the noisy data is normalized back with scale factor $C_{NP}(x,y,z)$ to maintain the Mean Variance Ratio (MVR) as K_{scale} [35].

$$CTS_{scale}(x,y,z) = K_{Scale} * \ CTS(x,y,z) \qquad (5)$$

$$\lambda(x,y,z) = \max\left(0, CTS_{scale}(x,y,z)\right) \qquad (6)$$

$$CTS_N(x,y,z) \sim Poisson\left(\lambda(x,y,z)\right); \quad P(CTS_{scale}(x,y,z) = a) = \frac{e^{-\lambda_{x,y,z}} * \lambda_{x,y,z}}{a!} \qquad (7)$$

$$C_{NP}(x,y,z) = \frac{CTS_N(x,y,z)}{K_{scale}} \qquad (8)$$

$$E[C_{NP}] = \frac{\lambda_{x,y,z}}{K_{scale}} \ \& \ Var(C_{NP}) = \frac{\lambda_{x,y,z}}{(K_{scale})^2} \qquad (9)$$

$$MVR_{Effective} = K_{scale} \qquad (10)$$

(e) Subsequently, the counts volume was converted back to activity concentration as reverse of step (c), then to simulate the inherent resolution limitations and some smoothing, an anisotropic Gaussian kernel was convolved with the activity map. This kernel was spatially variant (in radial direction), with its Full Width at Half Maximum (FWHM) dimensions derived from the scanner's performance specifications (Table.1) as per AAPM (American Association of Physicists in Medicine) Task Group 126 (TG-126) findings [43]. This choice was primarily driven by the absence of a simulated attenuation CT, which is typically required to accurately model the scattering effects. Detailed mathematical description and the values of FWHM used for gaussian model are included in supplementary information.

(f) An additional post processing gaussian (Eq. 8) is included as an optional filter to represent some reconstruction smoothing which is not utilized in this study.

To create a scanner and acquisition dependent dataset of the simulated noise, iterative variations of K_{scale} from 1 down to 0 were performed. For each value, a noisy simulated volume was generated. Mean Variance Ratio (MVR) for each generated sample, was computed using two distinct methods: a 2D region of interest (ROI) extraction across six randomly chosen uniform slices, and a 3D volume of interest (VOI) extraction for a 75mm uniform activity section from the center to top of the phantom. Based on extracted noise characteristics, a best fit between the calculated MVR and their corresponding K_{Scale} values was performed. This followed by determination of MVR for the acquisitions using in the same ROI and VOI approach to subsequently identify the corresponding K_{Scale} parameter from the noise fit that was applied across the 3 frames.

2.4 Data Extraction & Statistical Tests:

The PET volume was categorized into 3 different regions reference solution water, background cube and targets for data extraction. Quantitative data extraction were carried out using VOI (matching physical dimensions of the target) approach following workflow of [8,24] on Image Interpretation Software - Volume Viewer, PETVCAR® (*GE Healthcare, Chicagio, IL, USA*) for experimental and ISL data, MATALB for MuPET. The activity values in kBq/mL were extracted semi-automatically. Two quantitative metrics were calculated namely recovery coefficient (RC) to quantify the ability to recover true activity concentrations and target contrast ratio (TCR) to assesses the detectability of lesions against homogeneous cubes (This is analogous to TBR[1] the difference being the later does same quantification w.r.t native background around the void where as TCR uses the corresponding homogeneous cubes) using (Eq. 9 & 10).

[1] In this article, TBR is always used to refer the expected or theoretical value and TCR is always used for the measured value

$$RC_{(mean/max)} = \frac{\text{Activity concentration in target volume (Mean/Max)}}{\text{Theoretical activity concentration}} \quad (9)$$

$$TCR_{(mean/max)} = \frac{\text{Activity Concentration in target volume (Mean/Max)}}{\text{Activity Concentration in homogeneous cube (Mean)}} \quad (10)$$

$$\text{Coefficient of Variability (CoV)} = \frac{\text{Standard Deviation } (\sigma)}{\text{Mean } (\mu)} \text{ x } 100 \quad (11)$$

Additionally, CoV for the uniform regions was calculated using (Eq. 11), based on the extracted VOI data of acquisition and MuPET. Detailed statistical tests for the 3 quantitative metrics were not performed due lower target sample size of $N_{Sample} = 6$ for each set, Standard percentage error and Bland-Altman bias with limits of agreement were calculated.

To statistically analyse activity distributions, we performed two additional data extractions: an **ROI-based extraction** and an **activity profile extraction**. For the ROI a total of 13 circular ROI's – 9 (ϕ 30mm – In 9 cubes) and 4 (ϕ 20mm – In 4 background water) were placed automatically on central cross-sectional slice with targets. For the second, activity profiles were extracted along the central vertical axis for visual comparison. All the extracted activity data were initially checked for normality using Shapiro-wilk test. This followed by two sided Brown and Forsythe equal variance test [44] on the ROI data of acquisition (Acq) and MuPET chosen for its reduced dependence on normality. Finally, the activity profiles for MuPET vs Acq and MuPET vs ISL were followed up by appropriate ANOVA or Wilcoxon rank sum test (also known as Mann Whitney) [17,24] for assessment of central tendency driven statistical differences. All tests were performed with significance of $p < 0.05$ in JASP (*JASP Team, Netherlands*).

3. Results:

3.1. Phantom Acquisitions and Synthetic Lesion Insertion:

The observed Hounsfield units (HU) on the CT values of homogeneous cubes were 4.6 ± 4.8 (TBR ~ 2), 4.5 ± 3.5 (TBR ~ 2.5), 7.6 ± 4.3 (TBR ~ 3.33) falling within the range of water (3.1 ± 3.7) thus establishing good compatibility in addition to the non-explicit visibility of the targets on CT when viewed on abdominal windowing (**Fig 2.a, 2.b**). All different regions were captured effectively on the PET acquisition (PET Acq), with different contrasts visibly distinguishable (**Fig 2.c, 2.d)** demonstrating the efficacy of the PET system in delineating areas of varying activity concentration. Additionally, inserted synthetic lesions (ISL) also represented well enough the actual targets and the respective visual comparison based on target diameter is in (**Fig 2.c, 2.d).**

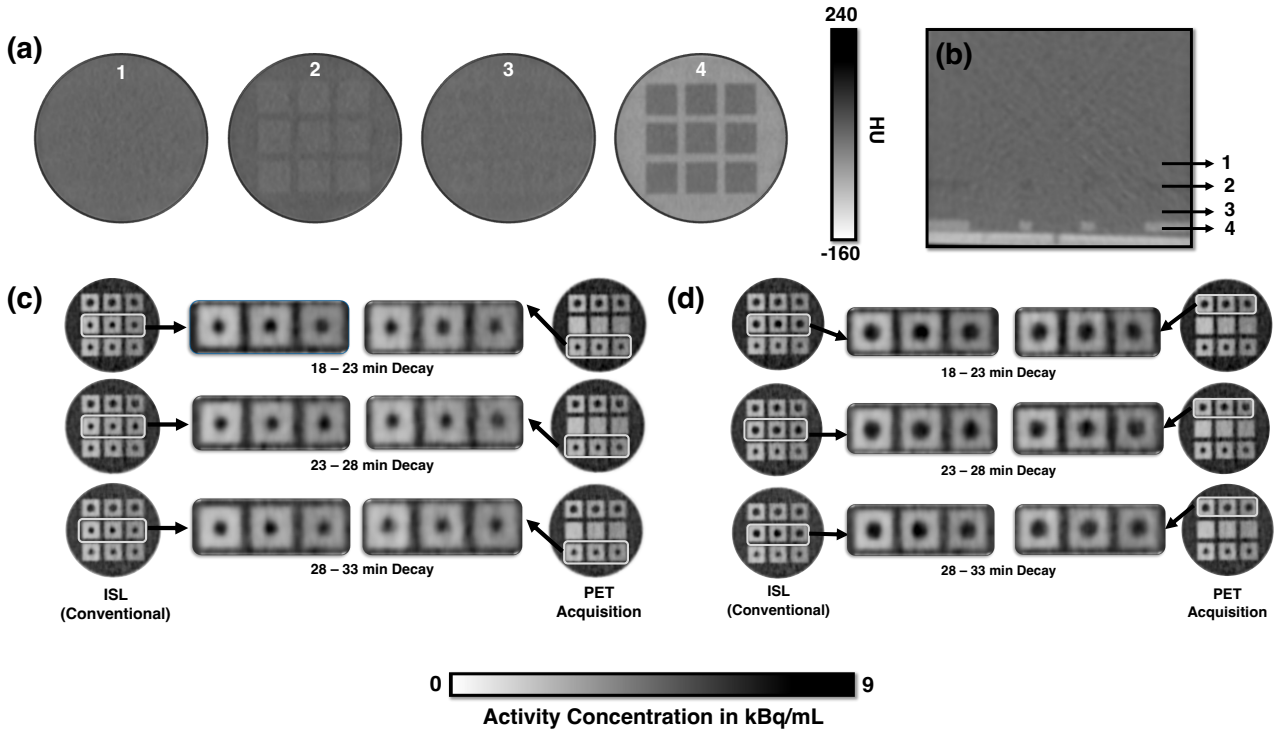

Fig.2 (a) Cross-sectional CT AC slices at 4 different locations (1. Pure Water, 2. ABS cubes with ABS support, 3. Cubes with water 4. ABS cubes with PLA support) **(b)** Corresponding location of CT slices; Central PET slice with exploded target view of ISL vs PET Acquisition for 3 frames **(c)** 15mm, **(d)** 20mm

3.2. Mass Diffusion and Decay Reaction Simulation:

The computational phantom, as depicted in **Fig. 3.a**, is estimated as 6.22 L volume. The volume average of activity concentration (kBq/mL) inside the computational phantom was multiplied based on this volume (mL) to determine the effectively activity (MBq) at each time step and was compared against the experimental values determined from decay corrected injected activity data as seen in (**Fig. 3.b**). The percentage differences observed for the activity were low, ranging only from 0.43% to 1.16% well within the margin of 5%. Regarding numerical stability, the grid discretization was observed to converge effectively within a range of 0.6 to 1 million tetrahedral elements (**Fig. 3.c**). Grid convergence for numerical simulations is crucial to ensure the independency of results on the grid resolution, thus enhancing the reliability of the simulation. Based on this analysis, 1 million tetrahedral elements were ultimately selected for the primary simulation analyses. This specific grid configuration resulted in computational time of ~ 10 minutes for a total simulated decay of 35 minutes (with a time step of 1 minute). Central cross-section of activity concentration for the 3 corresponding time steps are illustrated in (**Fig. 3.d**) with observed maximum – minimum values as 8.26 – 2.16, 8.10 – 2.13, 7.84 – 2.09 kBq/mL. This not only illustrates the decay of the tracer but also distinctly the clear transition boundaries between regions of differing activity concentrations, confirming the model's ability.

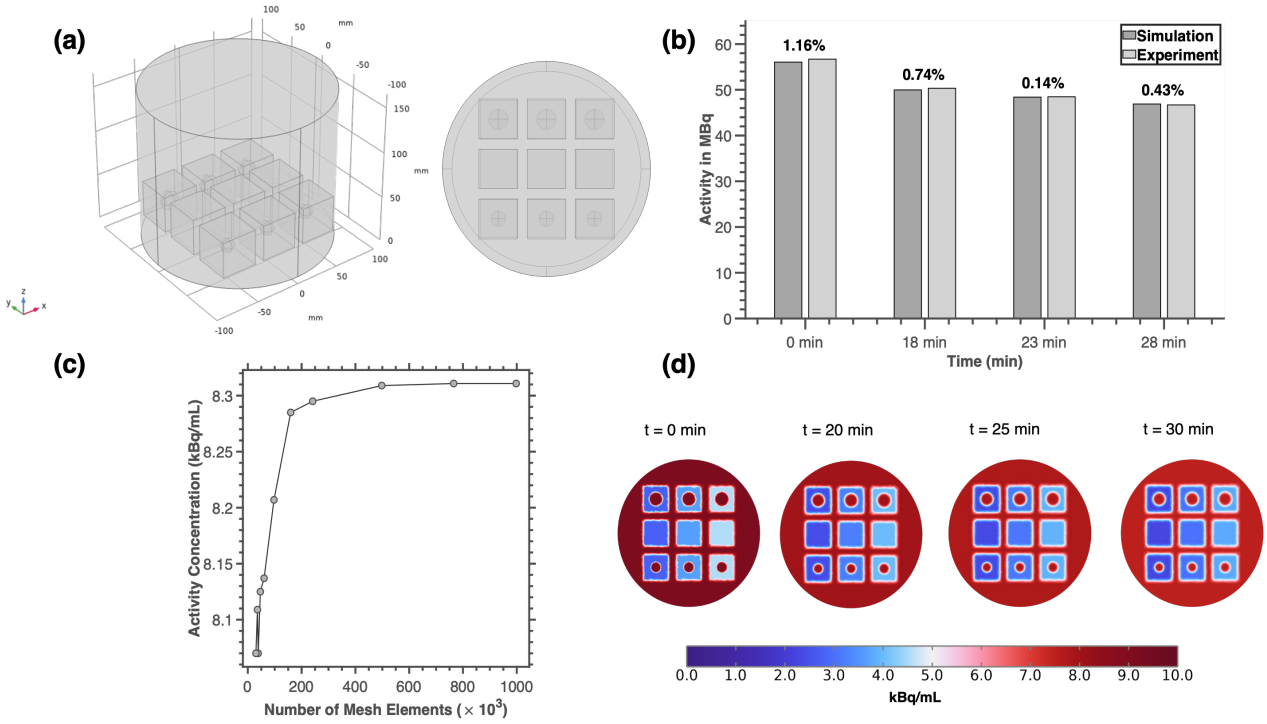

Fig.3 (a) 3D rendering of the computational domain and Axial (Top view) of geometric setup displaying targets and cubes following experimental layout **(b)** Comparison of effective activity (in MBq) of simulation with analytically calculated decay corrected activity from DICOM metadata; **(c)** Grid Convergence for simulation; **(d)** Central cross-sectional slice for simulated activity distribution at different time stamps prior to noise addition.

3.3. Noise characterization and MuPET modelling:

In the context of determining the noise model for the PET simulation, the $MVR_{Acquisition}$ determined from experimental PET data based on a central VOI measuring Φ 18 cm x 7.5 cm yielded a global value of 85.8. Additionally, MVR values extracted from ten random uniform slices, utilizing an 18 cm ROI [34], resulted in a consistent range of values between 75 - 95. Consequently, an average MVR of 85 was selected as the target value to accurately replicate the inherent noise. Various samples of simulated noise on the exported activity data constructed by varying K_{scale} between 0.005 to 1 for a fit (**Fig.4.a**) can be found in **Fig 4.b**. It is crucial to note that this fit is intrinsically specific to the particular scanner properties used in the scanner model. Utilizing this linear relationship, the most appropriate K_{Scale} parameter of 0.0415 resulted in MVR of ~ 85 which was used globally for the 3 frames (**Fig.4.c, 4.d**). Furthermore, the coefficient of variability (CoV) for the experimental and MuPET VOI data consistently remained well within acceptable 5% bounds.

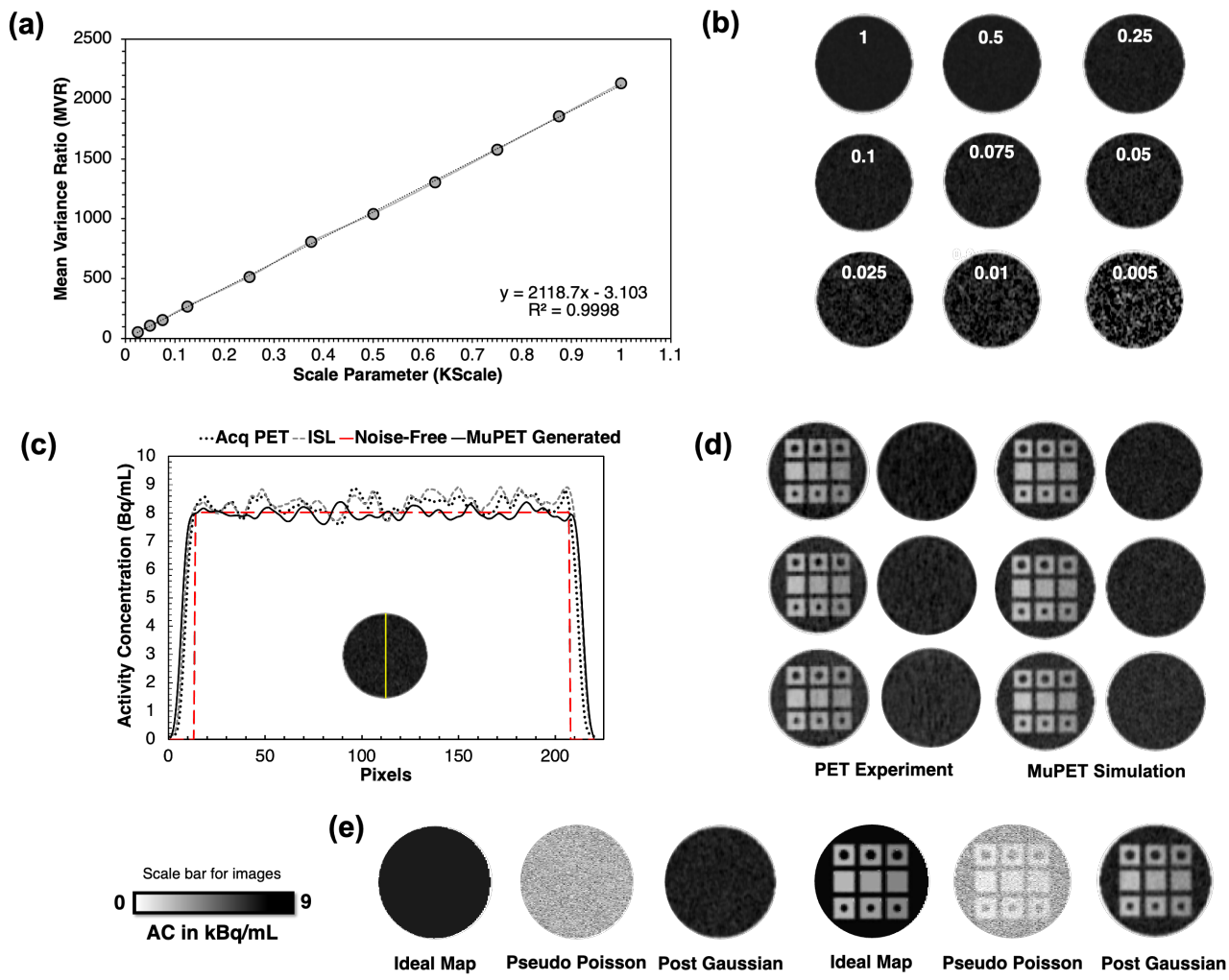

Fig.4 (a) Linear Fit for K_{Scale} as function of MVR for simulation map **(b)** Cross-sectional slice of generated noise for different K_{Scale} **(c)** Activity profile extracted experimental data, simulated map and corresponding generated noise for frame – 1 **(d)** Background and Target images of the 3 frames - Acquisition PET (COV_{BKG} – 3.75, 3.83, 3.91 %) vs MuPET simulation for K_{Scale} ~ 0.03 (COV_{BKG} – 3.63, 3.64, 3.75 %); **(e)** Overview of noise generation workflow for background and target slices

3.4. Quantitative Comparison for PET profiles and metrics:

Extracted vertical activity profiles on cross sectional slice, which graphically represent the distribution of radiotracer are clearly depicted in **Fig 5.a**. This illustrates the transition between multiple regions in PET image across different target sizes and contrasts with a strong qualitative agreement among these different profiles. Notably, for the targets, the profiles exhibit a Gaussian-like peak rather than a flat plateau (noise-free), which is characteristic of PVE (partial volume effects). Beyond visual assessment, quantitative metrics provided a deeper insight into the model's perfromance. RC and TCR averaged over 3 frames are presented in **Fig.5.b ,5.c & 5.d**. To statistically quantify the biases between the methodologies,

Bland-Altman bias analysis results are summarized in **Table. 1**, revealing that the ISL method generally tends to overestimate the maximum values when compared to acquired PET data. In contrast, MuPET exhibited underestimation of maximum values when measured against acquired PET. The mean values across all 3 methods were within same range of bias.

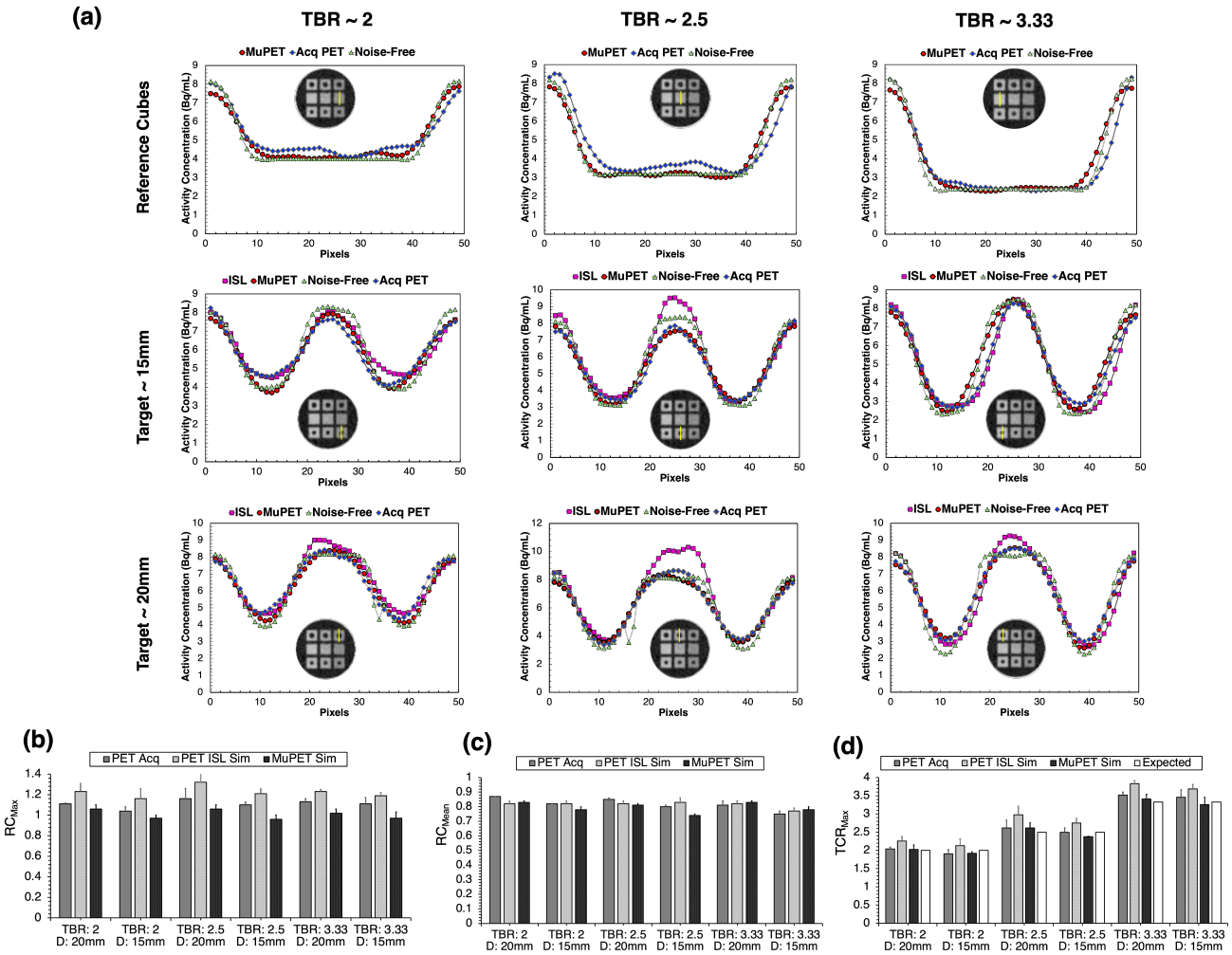

Fig.5 (a) Vertical activity profile of cubes on central cross-sectional slice for first frame – Homogeneous Cubes, 15- and 20-mm Targets (Rows); TBR ~ 2.00, 2.50, 3.33 (Columns); Averaged quantitative metrics comparison based on VOI data for **(b)** RC_{mean}, **(c)** RC_{max}, **(d)** TCR_{max} (Corresponding data can be found in supplementary information)

Table. 1 Bland Altman Mean Bias percentage with limits of acceptance (Mean ± 1.96 * SD) for Quantitative Metrics

Quantitative Metric	Acq vs ISL	Acq vs MuPET	ISL vs MuPET
RC_{max}	-9.84 ± 4.02	9.64 ± 6.98	10.27 ± 4.04
RC_{mean}	0.33 ± 7.29	2.66 ± 9.72	2.32 ± 9.99
TCR_{max}	-9.73 ± 4.29	2.34 ± 5.37	12.06 ± 2.94

Further validation from the analysis of region of interest (ROI) data, demonstrated that the mean activity concentrations for MuPET were within the variability range of acquired PET (**Table .2**). The extracted ROI data were fit using the Kernel Density Estimation (KDE) method and a jaccard overlap index (ratio of intersection over union), between the acquisition and MuPET was calculated and visually illustrated in **Fig.6**. For the statistical tests on ROI and activity profile data, Shapiro-Wilk p-values were consistently < 0.05 (Ranging between 0.01 - 1.79 x 10^{-25}; All values presented in supplementary information) indicating non-normal distribution, leading to the use of non-parametric statistical tests. Results of the follow up statistical tests are summarized in **Table 2**.

Table. 2 Summary of data descriptives & non-parametric statistical tests

		TBR ~ 3.33:1			TBR ~ 2.50:1			TBR ~ 2.00:1			Reference Solution
		R	15mm	20mm	R	15mm	20mm	R	15mm	20mm	
ROI Data	*Mean in kBq/mL (Coefficient of Variation %)*										
	Acq	2.44 (3%)	3.79 (40%)	4.62 (39%)	3.35 (4%)	4.42 (30%)	5.17 (29%)	4.16 (3%)	4.98 (19%)	5.49 (22%)	7.92 (3%)
	MuPET	2.32 (4%)	3.58 (42%)	4.56 (39%)	3.06 (4%)	4.13 (30%)	4.98 (31%)	3.93 (3%)	4.74 (21%)	5.44 (24%)	7.78 (2%)
	Brown Forsythe P – value: N_{Sample} ~ 17000 (For background), 990 (For rest)										
	-	0.01	0.75	0.85	0.45	0.69	0.63	0.63	0.49	0.08	0.001
Wilcoxon Rank Sum P – value: N_{Sample} ~ 442 (For background), 98 (For rest)											
Activity Profile (MuPET vs Acq)		0.91	0.79	0.80	0.001	0.97	0.72	0.008	0.69	0.54	0.05
Activity Profile (ISL vs Acq)		-	0.45	0.99	-	0.23	0.19	-	0.28	0.27	0.00135

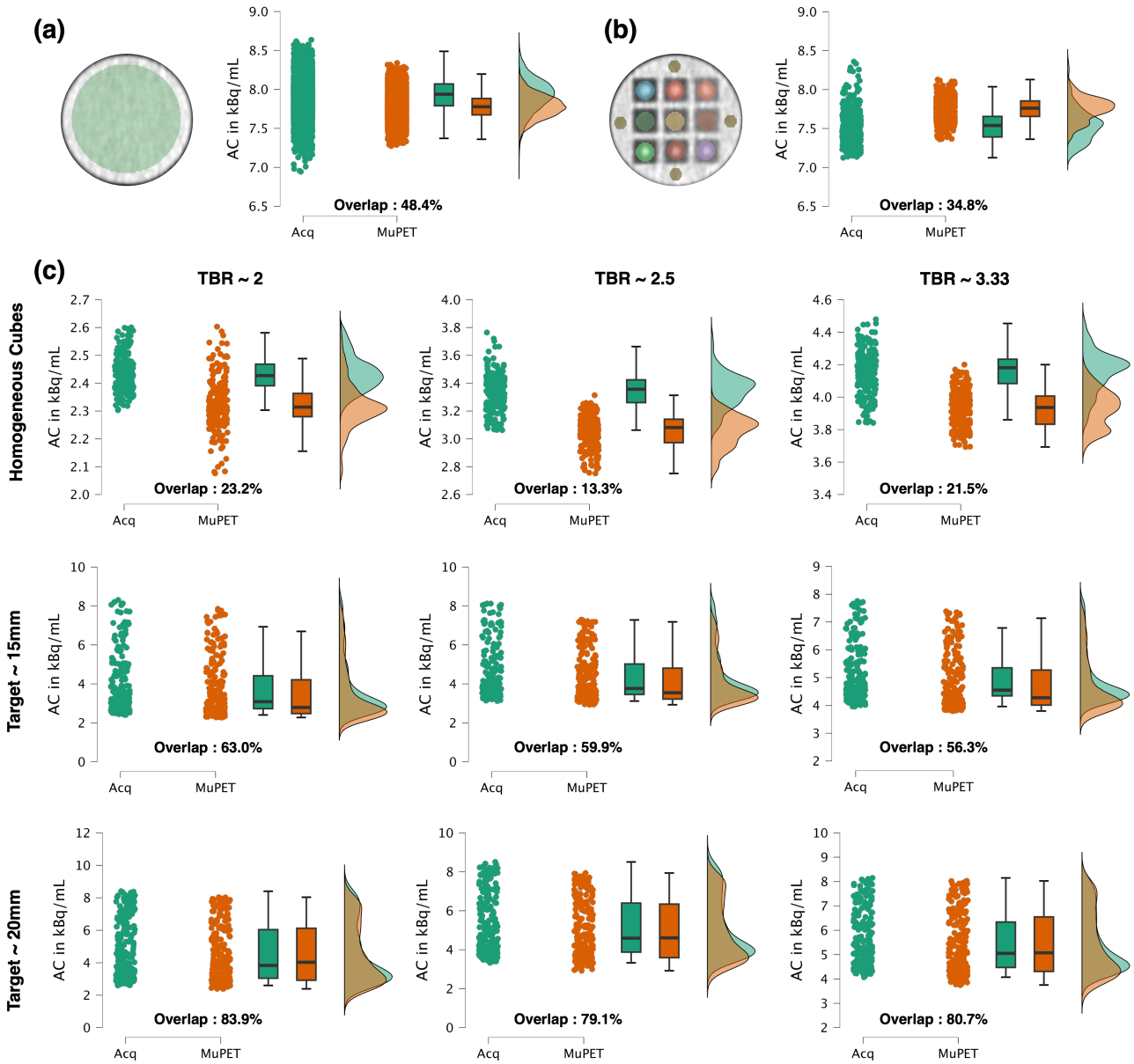

Fig.6 (a) Extracted activity distribution for 18cm ROI on Uniform slice for MuPET vs Acq; **(b)** ROI placement (30mm for cubes, 20mm for water) and corresponding data distribution comparison for water ROIs; **(c)** Corresponding comparison of raincloud data distribution plots for cubes - Reference Cubes, 15- and 20-mm Targets (Rows); TBR ~ 2.00, 2.50, 3.33 (Columns).

4. Discussion:

The MuPET framework, as introduced in this work, represents generating synthetic PET data that closely mimics real-world phantom acquisitions. This novel approach integrates diffusion-reaction modelling with a pseudo-poisson noise model and scanner-specific resolution blurring. Our mass diffusion model, despite several approximations, effectively represents the tracer distribution. This is crucially validated by the qualitative and quantitative agreement between

the simulated effective activity (**Fig. 3.b**) and the noise-free target activity profiles (**Fig. 3.d**), which follow experimental patterns. A key approximation in our modelling is the assumption of bulk concentrations instead of simulating the injection and uptake. This approximation is supported by the phantom design where the cube's intricate design (pores typically < 1mm) alters the micro-level tracer distribution but the average macroscopic behaviour is captured on the PET image. This is due to the design parameters being lower than scanner spatial resolution [8,9]. This reduces the computational intensity by avoiding high refinement zones within the geometry. Though, such an approximation might not hold true if active movement of tracer (coupled with flow physics) is to be included where convection overplays diffusion [45]. While we currently assume the diffusion properties of the ABS cubes are identical to water + FDG, this is far from reality. In the physical phantom, the actual concentration gradients are affected by geometrical variations [46]. The true diffusivity in the cubes is much lower than a bulk volume of adjusted concentration. Consequently, using water's diffusion properties in simulations, especially those with extended decay periods, risks overestimating the actual diffusion. Especially, such an assumption would not hold for materials with density significantly different than water. A robust solution with this regard is to build an empirical dataset following homogenization principles [46,47], where microscopic changes in permeability and diffusivity are mapped to a macroscopic value as a function of porosity. Such a dataset is easily compatible with flow physics, making adaptability for dynamic simulations easier. Additionally, anisotropic effects can also be added. Previous works deploying similar modelling approach were mostly used only for simulating time-activity curves without any noise addition [28,45].

Moving to the noise model, the primary goal was to mimic quantitative noise than textural. Traditional poisson noise models fall short to accurately replicate the observed variance in actual PET images [34,37], hence a pseudo scaled poisson noise [35] was utilised with controllable mean to variance ratio. While the combination of pseudo-poisson with subsequent blurring generates images with textures similar to observed in PET imaging, the acquisition visual texture is distinct for various regions. The approximated noise model seemed to accurately represent the quantitative metrics closer to the experiment though with some discrepancies (**Table.1 & Fig. 5**). Both RC and TCR are within the ranges of the original phantoms design studies [8,17]. Across all evaluated target sizes, MuPET showed strong alignment with both acquisition and ISL for TCR_{max} and $RC_{mean.}$. This is also supported by the close activity profiles (**Fig. 5.b**) to the experiment and ISL. The resulting p-values also signify the absence of statistical evidence though with some outliers. But to accurately determine the PVE, a detailed analysis based on a common segmentation criteria as performed in [21] would be ideal than 2D profiles. Notably, the conventional synthetic lesion insertion method was found to be consistently overestimating the values especially RC_{max} & TCR_{max}. This is because applying a user-defined contrast ratio to a base experimental scan, which inherently carries a PET noise bias for 3D-printed grid designs [8,9], multiplies the bias leading to overestimation.

Such overestimation was not observed for conventional QC phantoms [23,24]. This highlights the limitation with respect to 3D printable designs, particularly for very high target-to-background ratios (TBRs), the workflow becomes challenging due to printing limitations as certain porosity levels cannot be reached [8]. In contrast, MuPET noise model showed underestimation of max values compared to the experiment (**Table 1**), which we attribute to two main factors: the simulation being instantaneous while experimental scans are acquired over time, and global application of the noise scaling parameter (K_{scale}) despite noise naturally increasing as counts decrease. The former can be addressed by selecting the last timestamp or an average across time stamps corresponding to the scan duration instead of an intermediate time point. The latter requires that the further iterations incorporate dependence of K_{scale} on count levels i.e. tailored to each frame. Additionally, while we followed the noise characterization approach of [34], the MVR remains sensitive to the chosen ROI or VOI; a more robust analysis like Noise Power Spectrum (NPS) analysis [21,33] or automatic slice by slice noise mapping [48] could better determine the noise characteristics. Another interesting phenomenon observed was that the overlap between extracted ROI activity histograms is the worst for homogeneous cubes and the targets provided the best representation. This accurate depiction of lesions is particularly promising, especially given that our noise model was generated based on uniform, non-target slices / ROIs. Interestingly, as shown in **Table. 2**, the Brown-Forsythe test indicated no statistically evidence in variances, except for the 50% reference cube and uniform slice. The higher COV for target cubes were because the ROI (30 mm) includes target and certain regions of background, to have consistent measurement across methods for comparison. In this framework the mean values are generally affected by the simulation and the max values by the variance in the noise model. Furthermore, for the homogeneous cubes, the ROI mean values are also underestimated because the framework doesn't include reconstruction effects. Specifically, BPL reconstruction algorithm used in acquisitions actively suppresses noise levels in low activity regions [23,24] i.e. the homogeneous cubes which is not captured by simple noise model. The integration of a spatially varying gaussian constituted as a key strength but should be adapted to FWHM of various reconstruction algorithms. The deliberate decision to model noise and resolution in image domain as opposed to sinogram was a pragmatic choice with the approach avoiding complexities of computation. Also, random, dead time and scatter effects are not individually considered and the performance of MuPET for extended decay where diffusion i.e. scatter becomes predominant is to be tested. However, the framework is intentionally designed with modularity allowing for future iterations including more accurate noise models.

In this work, our primary objective was to establish a faster and flexible computational pipeline specifically tailored for testing and optimizing design of novel phantom features. Unlike conventional lesion insertion methods that rely on prior prototyping or readily available digital phantoms, MuPET emphasizes on modelling tracer distributions. This leads to a total computation time of less than 15 minutes for entire pipeline from simulating activity map to generation of

PET data for all frames. This compared to ISL which took approximately 12 hours for 3 frames. That being said, this framework is not intended to serve as a replacement for existing methods which are more closer to PET clinical applications. While, MuPET provides quantitively closer results for initial benchmarking, it consciously incorporates trade-offs to achieve computational speed. An interesting addition for future works would be a sinogram based pipeline with an approximated CT attenuation map based on [49]. This enables the potential to include reconstruction algorithms thus reducing on empirically derived relations, opening avenues for comprehensive image quality studies. Also, potentially MuPET has to be benchmarked against standardised phantoms with fillable acrylic sphere targets such as NEMA IEC body phantom [24] for which data for various reconstruction algorithms is available. This can aid in having a more robust noise approximation model. Despite these acknowledged limitation due to its inherent computational efficiency, combined with its flexibility in handling complex geometries makes MuPET adaptable and accessible for wide spectrum of research.

Conclusion:

The MuPET framework successfully introduces a computationally efficient method for generating realistic synthetic PET data, a crucial advancement for the design and evaluation of 3D-printed phantoms. By integrating multiphysics modelling with an empirical noise model, MuPET accurately predicts tracer distributions and replicates certain aspects of scanner noise. This approach, validated by strong agreement with experimental data and conventional lesion insertion methods significantly accelerates the design and optimization of novel phantoms, offering a cost-effective alternative prior to physical prototyping in PET imaging research.

References:

1. Engbersen MP, Van Driel W, Lambregts D, Lahaye M. The role of CT, PET-CT, and MRI in ovarian cancer. Br J Radiol. 2021;94:20210117.

2. Hadebe B, Harry L, Ebrahim T, Pillay V, Vorster M. The Role of PET/CT in Breast Cancer. Diagnostics. 2023;13:597.

3. Alberts I, Hünermund J-N, Prenosil G, Mingels C, Bohn KP, Viscione M, et al. Clinical performance of long axial field of view PET/CT: a head-to-head intra-individual comparison of the Biograph Vision Quadra with the Biograph Vision PET/CT. Eur J Nucl Med Mol Imaging. 2021;48:2395–404.

4. Koole M, Armstrong I, Krizsan AK, Stromvall A, Visvikis D, Sattler B, et al. EANM guidelines for PET-CT and PET-MR routine quality control. Z Für Med Phys. 2023;33:103–13.

5. Aide N, Lasnon C, Veit-Haibach P, Sera T, Sattler B, Boellaard R. EANM/EARL harmonization strategies in PET quantification: from daily practice to multicentre oncological studies. Eur J Nucl Med Mol Imaging. 2017;44:17–31.

6. Matheoud R, Boellaard R, Pike L, Ptacek J, Reynés-Llompart G, Soret M, et al. EFOMP's protocol quality controls in PET/CT and PET/MR. Phys Med. 2023;105:102506.

7. Sagara H, Inoue K, Mano C, Kajiwara H, Nagai Y, Fujii H, et al. Usefulness of a new anthropomorphic phantom simulating the chest and abdomen regions in PET tests. Ann Nucl Med. 2025;39:303–12.

8. Nalla SKK, Maronnier Q, Hazan TP, Kennedy J, Caselles O. Enhancing PET/CT Assessment with Porous 3D Printed Grids: A Pilot Study [Internet]. medRxiv; 2025 [cited 2025 Apr 2]. p. 2025.04.01.25325022. Available from: https://www.medrxiv.org/content/10.1101/2025.04.01.25325022v1

9. Jessen L, Gustafsson J, Ljungberg M, Curkic-Kapidzic S, Imsirovic M, Sjögreen-Gleisner K. 3D printed non-uniform anthropomorphic phantoms for quantitative SPECT. EJNMMI Phys. 2024;11:8.

10. Gear JI, Long C, Rushforth D, Chittenden SJ, Cummings C, Flux GD. Development of patient-specific molecular imaging phantoms using a 3D printer. Med Phys. 2014;41:082502.

11. Gear JI, Cummings C, Sullivan J, Cooper-Rayner N, Downs P, Murray I, et al. Radioactive 3D printing for the production of molecular imaging phantoms. Phys Med Biol. 2020;65:175019.

12. Zounek AJ, Joerg NM, Lindheimer F, Zatcepin A, Palumbo G, Oos R, et al. 3D printing of radioactive wall-less PET phantoms improves threshold-based target delineation and quantification. EJNMMI Phys. 2025;12:53.

13. Gallivanone F, Interlenghi M, D'Ambrosio D, Trifirò G, Castiglioni I. Parameters Influencing PET Imaging Features: A Phantom Study with Irregular and Heterogeneous Synthetic Lesions. Contrast Media Mol Imaging. 2018;2018:5324517.

14. Alsyed E, Smith R, Bartley L, Marshall C, Spezi E. A heterogeneous phantom study for investigating the stability of PET images radiomic features with varying reconstruction settings. Front Nucl Med [Internet]. 2023 [cited 2025 Apr 27];3. Available from: https://www.frontiersin.orghttps://www.frontiersin.org/journals/nuclear-medicine/articles/10.3389/fnume.2023.1078536/full

15. Carles M, Fechter T, Martí-Bonmatí L, Baltas D, Mix M. Experimental phantom evaluation to identify robust positron emission tomography (PET) radiomic features. EJNMMI Phys. 2021;8:46.

16. Pfaehler E, Sluis J van, Merema BBJ, Ooijen P van, Berendsen RCM, Velden FHP van, et al. Experimental Multicenter and Multivendor Evaluation of the Performance of PET Radiomic Features Using 3-Dimensionally Printed Phantom Inserts. J Nucl Med. 2020;61:469–76.

17. Nalla SKK, Maronnier Q, Palchan-Hazan T, Caselles O, Kennedy J. Facilitating Multi-Center Consistency in PET/CT Assessment: Transferability and Harmonization of 3D-Printed Phantom Inserts [Internet]. medRxiv; 2025 [cited 2025 June 1]. p. 2025.05.30.25328639. Available from: https://www.medrxiv.org/content/10.1101/2025.05.30.25328639v1

18. Jessen L, Curkic Kapidzic S, Gustafsson J, Larsson E, Ljungberg M, Sandström M, et al. A validation protocol for 177Lu-SPECT image quantification as a basis for multi-centre kidney dosimetry. Phys Med Biol. 2025;70:115001.

19. Baum KG, Helguera M. Execution of the SimSET Monte Carlo PET/SPECT Simulator in the Condor Distributed Computing Environment. J Digit Imaging. 2007;20:72–82.

20. Pfaehler E, De Jong JR, Dierckx RAJO, van Velden FHP, Boellaard R. SMART (SiMulAtion and ReconsTruction) PET: an efficient PET simulation-reconstruction tool. EJNMMI Phys. 2018;5:16.

21. Li S, Hamdi M, Dutta K, Fraum T, Luo J, Laforest R, et al. FAST (fast analytical simulator of tracer)-PET: an accurate and efficient PET analytical simulation tool. Phys Med Biol. 2024;69.

22. Berthon B, Häggström I, Apte A, Beattie BJ, Kirov AS, Humm JL, et al. PETSTEP: Generation of synthetic PET lesions for fast evaluation of segmentation methods. Phys Med. 2015;31:969–80.

23. Wangerin KA, Ahn S, Wollenweber S, Ross SG, Kinahan PE, Manjeshwar RM. Evaluation of lesion detectability in positron emission tomography when using a convergent penalized likelihood image reconstruction method. J Med Imaging. 2016;4:011002.

24. Maronnier Q, Courbon F, Caselles O. Evaluation of a method based on synthetic data inserted into raw data prior to reconstruction for the assessment of PET scanners. EJNMMI Phys. 2022;9:68.

25. Peladeau-Pigeon M. Simulation of Perfusion Flow Dynamics for Contrast Enhanced Imaging. 2012 [cited 2025 June 1]; Available from: http://hdl.handle.net/1807/33495

26. Haroun S, Wang L, Ruth TJ, Li PCH. Computational fluid dynamics study of the synthesis process for a PET radiotracer compound, [11C]raclopride on a microfluidic chip. Chem Eng Process Process Intensif. 2013;70:140–7.

27. Dimitrakopoulou-Strauss A, Pan L, Sachpekidis C. Kinetic modeling and parametric imaging with dynamic PET for oncological applications: general considerations, current clinical applications, and future perspectives. Eur J Nucl Med Mol Imaging. 2021;48:21–39.

28. Kamphuis ME, Kuipers H, Verschoor J, Van Hespen JCG, Greuter MJW, Slart RHJA, et al. Development of a dynamic myocardial perfusion phantom model for tracer kinetic measurements. EJNMMI Phys. 2022;9:31.

29. Siekkinen R, Teuho J, Smith NAS, Fenwick A, Kirjavainen AK, Koskensalo K, et al. Study of the Effect of Reconstruction Parameters for Myocardial Perfusion Imaging in PET With a Novel Flow Phantom. Front Phys [Internet]. 2020 [cited 2025 June 18];8. Available from: https://www.frontiersin.org/journals/physics/articles/10.3389/fphy.2020.00148/full

30. Abazari MA, Soltani M, Eydi F, Rahmim A, Kashkooli FM. Mathematical modeling of 18F-Fluoromisonidazole (18F-FMISO) radiopharmaceutical transport in vascularized solid tumors. Biomed Phys Eng Express. 2024;10:065014.

31. Kashkooli FM, Abazari MA, Soltani M, Ghazani MA, Rahmim A. A spatiotemporal multi-scale computational model for FDG PET imaging at different stages of tumor growth and angiogenesis. Sci Rep. 2022;12:10062.

32. Kiani Shahvandi M, Soltani M, Moradi Kashkooli F, Saboury B, Rahmim A. Spatiotemporal multi-scale modeling of radiopharmaceutical distributions in vascularized solid tumors. Sci Rep. 2022;12:14582.

33. Castro P, Huerga C, Chamorro P, Garayoa J, Roch M, Pérez L. Caracterización y simulación de ruido en las imágenes de PET reconstruidas con OSEM: desarrollo de un método para la generación de imágenes sintéticas. Rev Esp Med Nucl E Imagen Mol. 2018;37:229–36.

34. Teymurazyan A, Riauka T, Jans H-S, Robinson D. Properties of Noise in Positron Emission Tomography Images Reconstructed with Filtered-Backprojection and Row-Action Maximum Likelihood Algorithm. J Digit Imaging. 2013;26:447–56.

35. Rowe RW, Dai S. A pseudo-Poisson noise model for simulation of positron emission tomographic projection data. Med Phys. 1992;19:1113–9.

36. Tong S, Alessio AM, Kinahan PE. Noise and signal properties in PSF-based fully 3D PET image reconstruction: an experimental evaluation. Phys Med Biol. 2010;55:1453.

37. Matheson GJ, Ge L, Zhang M, Sun B, Tu Y, Zanderigo F, et al. Parametric and non-parametric Poisson regression for modelling of the arterial input function in positron emission tomography. EJNMMI Phys. 2023;10:72.

38. Mou T, Huang J, O'Sullivan F. The Gamma Characteristic of Reconstructed PET Images: Implications for ROI Analysis. IEEE Trans Med Imaging. 2018;37:1092–102.

39. de Bourbon Q, Ahamed S, Blanc-Durand P, Rahmim A, Klein R. Characterization of artificial intelligence performance for lesion detection using synthetic lesions in PET imaging. Med Phys. 2025;52:3994–4007.

40. Kreft M, Lukšič M, Zorec TM, Prebil M, Zorec R. Diffusion of d-glucose measured in the cytosol of a single astrocyte. Cell Mol Life Sci CMLS. 2012;70:1483–92.

41. IAEA Human Health Series 2009 No. 1. Quality Assurance for PET and PET/CT Systems. Vienna, IAEA, 2009 [Internet]. [cited 2025 Apr 9]. Available from: https://www.researchgate.net/publication/274082148_IAEA_Human_Health_Series_2009_No_1_Quality_Assurance_for_PET_and_PETCT_Systems_Vienna_IAEA_2009

42. Pan T, Einstein SA, Kappadath SC, Grogg KS, Lois Gomez C, Alessio AM, et al. Performance evaluation of the 5-Ring GE Discovery MI PET/CT system using the national electrical manufacturers association NU 2-2012 Standard. Med Phys. 2019;46:3025–33.

43. AlMazrou RY, Alanazi SF, Alzaid MH, Al-Fakhranee RS, Ding S, Mawlawi OR. Performance characteristics of the 5-ring GE Discovery MI PET/CT scanner using AAPM TG-126 report. J Appl Clin Med Phys. 2024;25:e14315.

44. Rogerson PA. Statistical tests for the local spatial variance. Int J Geogr Inf Sci. 2022;36:1503–17.

45. Peladeau-Pigeon M, Coolens C. Computational fluid dynamics modelling of perfusion measurements in dynamic contrast-enhanced computed tomography: development, validation and clinical applications. Phys Med Biol. 2013;58:6111.

46. Karuna C, Poltue T, Khrueaduangkham S, Promoppatum P. Mechanical and fluid characteristics of triply periodic minimal surface bone scaffolds under various functionally graded strategies. J Comput Des Eng. 2022;9:1258–78.

47. Asbai-Ghoudan R, Ruiz de Galarreta S, Rodriguez-Florez N. Analytical model for the prediction of permeability of triply periodic minimal surfaces. J Mech Behav Biomed Mater. 2021;124:104804.

48. Sartoretti T, Skawran S, Gennari AG, Maurer A, Euler A, Treyer V, et al. Fully automated computational measurement of noise in positron emission tomography. Eur Radiol. 2024;34:1716–23.

49. Douglass MJJ. An open-source tool for converting 3D mesh volumes into synthetic DICOM CT images for medical physics research. Phys Eng Sci Med [Internet]. 2025 [cited 2025 July 31]; Available from: https://doi.org/10.1007/s13246-025-01599-x

Disclosures:

MuPET framework is developed as part of research collaboration partnership between the teams of Olivier Caselles and Sebastian Uppapalli. The authors declare that no funds, grants, or other support were received during the preparation of this manuscript. The authors also declare no conflict of interest.

Supplementary Information:

Mathematical Model of Spatially Variant Gaussian Filter: This section details the mathematical model underlying the simulation of spatially variant and anisotropic blurring. The primary objective of this model is to transform a noisy activity distribution into a representation that closely approximates the resolution properties observed in real PET acquisitions. At its fundamental level, the blurring effect introduced by an imaging system can be effectively approximated as a convolution operation with a Point Spread Function (PSF). For a 3D volumetric input activity distribution, denoted as $AC_{input}(x,y,z,t)$, the resulting blurred distribution, $AC_{blurred}(x,y,z,t)$, is obtained through the following convolution using *imgaussfilt3* in MATLAB:

$$A_{Blurred} = A_{input} * G(x, y, z, \sigma_x, \sigma_y, \sigma_z)$$

Where * is convolution and G is the gaussian function. The Gaussian function is a widely adopted and computationally efficient model for the PSF due to its analytical tractability and its good approximation of the central lobe of many real imaging system responses. The mathematical formulation of the 3D Gaussian kernel is given by:

$$G(x, y, z, \sigma_x, \sigma_y, \sigma_z) = \frac{e^{(-0.5 \times (\frac{x^2}{\sigma_x{}^2} + \frac{y^2}{\sigma_y{}^2} + \frac{z^2}{\sigma_z{}^2}))}}{\sqrt{(2\pi)^3 (\sigma_x \times \sigma_y \times \sigma_z)^2}}$$

In this equation, σ_x, σ_y, and σ_z represent the standard deviations of the Gaussian function along the x, y, and z axes, respectively. These standard deviations directly dictate the extent of blurring applied in each corresponding direction; a larger σ value indicates a wider Gaussian curve and thus more pronounced blurring. The resolution characteristics of a PET scanner are often anisotropic, meaning that the degree of blurring is not uniform across all spatial directions. In this model, the blurring is specifically anisotropic, with distinct standard deviations applied along the primary axes, with the directions are approximated as Radial Direction: governed by σ_x, Tangential Direction: governed by σ_y, and Axial Direction: governed by σ_z. The standard deviation (σ) for each direction is derived from the Full Width at Half Maximum (FWHM) values, which are obtained from predefined scanner-specific performance data (Table S1). The conversion from FWHM to σ is established by the following relationship:

$$\sigma = \frac{FWHM}{2\sqrt{2\ln(2)}} = \frac{FWHM}{2.3548}$$

Ideally, spatially variant blurring implies that the standard deviations (σ) of the Gaussian kernel would continuously change based on the exact spatial position x within the volume, i.e., G(x,σ(x)). Implementing such voxel to voxel, continuous variation is computationally very demanding. To address this, the model employs a practical and computationally efficient approximation by segmenting the spatial domain into **radial zones**. The 3D volume is conceptually divided into concentric cylindrical shells, or zones, based on their radial distance from the scanner's central axis (isocenter). For each defined zone, a representative radius (typically the midpoint between its inner and outer boundaries) is selected. This representative radius serves as the basis for determining the blurring parameters within that specific zone. The FWHM values for the radial, tangential, and axial directions are interpolated from the scanner's empirical resolution data points (e.g., at various radial distances from the isocenter i.e 1 cm, 10 cm, 20 cm) at the respective representative radii of each zone. These interpolated FWHM values are then converted into pixel-based σ_x, σ_y, σ_z values, which are unique to each specific zone. Gaussian was applied individually for each zone and then combined back into final volume.

Table. S1 Scanner Parameters used for the Noise Model adapted from NEMA and APA data

Sensitivity in cps/kBq	20.08
1 cm FWHM (Radial, Tangential, Axial) in mm	4.08, 4.39, 4.57
10 cm FWHM (Radial, Tangential, Axial) in mm	4.59, 3.99, 4.75
20 cm FWHM (Radial, Tangential, Axial) in mm	7.01, 4.78, 4.56
Scan Duration in seconds	300
Voxel Volume in mL	0.00304

Table. S2 Quantitative Metrics calculated for VOI data extracted

Designed Target to Background Ratio	Target Diameter (mm)	Acquired PET; Inserted Synthetic Lesion on Acquired PET; MuPET Simulation (Mean ± SD)			
		RC_{Mean}	RC_{Max}	TCR_{Max}	TCR_{Mean}
2 : 1	**20**	0.87 ± 0.00; 0.82 ± 0.02; 0.83 ± 0.01	1.11 ± 0.01; 1.23 ± 0.08; 1.06 ± 0.04	2.04 ± 0.05; 2.26 ± 0.12; 2.03 ± 0.12	1.58 ± 0.01; 1.68 ± 0.00; 1.55 ± 0.01
	15	0.82 ± 0.00; 0.82 ± 0.02; 0.78 ± 0.02	1.04 ± 0.04; 1.16 ± 0.10; 0.97 ± 0.03	1.91 ± 0.11; 2.13 ± 0.18; 1.92 ± 0.04	1.50 ± 0.05; 1.68 ± 0.03; 1.63 ± 0.03
2.5 : 1	**20**	0.85 ± 0.01; 0.82 ± 0.02; 0.81 ± 0.01	1.16 ± 0.10; 1.32 ± 0.10; 1.06 ± 0.04	2.62 ± 0.21; 2.98 ± 0.23; 2.62 ± 0.14	1.90 ± 0.03; 2.03 ± 0.01; 1.99 ± 0.06
	15	0.80 ± 0.01; 0.83 ± 0.03; 0.74 ± 0.01	1.10 ± 0.03; 1.21 ± 0.05; 0.96 ± 0.04	2.50 ± 0.12; 2.75 ± 0.13; 2.38 ± 0.01	1.80 ± 0.08; 1.86 ± 0.04; 1.83 ± 0.04
3.33 : 1	**20**	0.81 ± 0.03; 0.82 ± 0.02; 0.83 ± 0.01	1.13 ± 0.03; 1.23 ± 0.02; 1.02 ± 0.04	3.52 ± 0.08; 3.83 ± 0.08; 3.41 ± 0.13	2.49 ± 0.06; 2.60 ± 0.01; 2.57 ± 0.04
	15	0.75 ± 0.02; 0.77 ± 0.02; 0.78 ± 0.02	1.11 ± 0.06; 1.19 ± 0.03; 0.97 ± 0.06	3.46 ± 0.20; 3.69 ± 0.12; 3.26 ± 0.20	2.32 ± 0.08; 2.36 ± 0.02; 2.35 ± 0.08

Table. S3 Shapiro – Wilk Normality Test P-values for Acquired PET

Designed Target to Background Ratio	Target Diameter (mm)	Shapiro – Wilk Normality Test P-values	
		Activity Profile Data	ROI Data
2 : 1	20	1.55e-3	1.27e-13
	15	5.95e-3	5.41e-17
	0	1.49e-7	4.84e-4
2.5 : 1	20	1.71e-3	1.77e-13
	15	2.92e-4	1.4e-17
	0	2.89e-8	9.18e-3
3.33 : 1	20	7.69e-4	3.12e-14
	15	3.69e-4	6.6e-18
	0	1.11e-8	1.63e-4
Bkg		1.26e-26	1.51e-8

Table. S4 Shapiro – Wilk Normality Test P-values for MuPET

Designed Target to Background Ratio	Target Diameter (mm)	Shapiro – Wilk Normality Test P-values	
		Activity Profile Data	ROI Data
2 : 1	20	1.39e-3	5.12e-12
	15	1.45e-3	1.70e-16
	0	5.09e-8	7.4e-4
2.5 : 1	20	3.99e-4	8.59e-12
	15	4.96e-4	1.29e-16
	0	1.64e-8	1.19e-4
3.33 : 1	20	3.45e-3	1.27e-12
	15	1.38e-3	1.07e-17
	0	3.53e-8	1.4e-6
Bkg		1.79e-25	1.87e-3

Table. S5 Shapiro – Wilk Normality Test P-values for ISL

Designed Target to Background Ratio	Target Diameter (mm)	Shapiro – Wilk Normality Test P-values	
		Activity Profile Data	ROI Data
2 : 1	20	1.45e-3	-
	15	1.92e-4	-
2.5 : 1	20	1.02e-3	-
	15	7.69e-4	-
3.33 : 1	20	6.98e-4	-
	15	9.5e-5	-
Bkg		1.79e-25	-